

Available online at www.sciencedirect.com

jmr&t
Journal of Materials Research and Technology
journal homepage: www.elsevier.com/locate/jmrt



Comparative performance evaluation of microarchitected lattices processed via SLS, MJ, and DLP 3D printing methods: Experimental investigation and modelling

Johannes Schneider ^a, S. Kumar ^{a,b,*}

^a Materials & Manufacturing Research Group, James Watt School of Engineering, University of Glasgow, Glasgow G12 8QQ, UK

^b Glasgow Computational Engineering Centre, University of Glasgow, Glasgow G12 8LT, UK

ARTICLE INFO

Article history:

Received 29 May 2023

Accepted 7 September 2023

Available online 12 September 2023

Keywords:

Additive manufacturing

Lattice structures

Architected materials

Energy absorption

Finite element modelling

ABSTRACT

Additively manufactured mechanical metamaterials are gaining prominence in lightweight energy-absorption applications due to their exceptional mass-specific properties. Herein, we examine the energy absorption characteristics of micro-architected truss-, shell- and plate-lattice structures, namely, Octet, Kelvin, Gyroid, SC, BCC and FCC over a range of relative densities under quasi-static compression via both experiments and finite element analysis (FEA). Employing different 3D printing methods, namely, Digital Light Processing, Selective Laser Sintering and Material Jetting, the lattices were fabricated using PlasGray™ (photo-resin based plastic), PA12 (Nylon) and VeroWhite (photo-resin based rigid plastic) respectively. Our results indicate that the SC lattice structure outperforms in terms of stiffness and strength, while the Gyroid lattice outperforms in terms of energy absorption efficiency (η). At lower relative densities (<0.3), η reaches up to 61% for the Gyroid lattices made of PlasGray, while only at high relative densities the Octet truss lattices compete with the Gyroid lattices. For Gyroid lattices made of PA12 with a relative density of 0.23, an energy absorption efficiency of 68% was observed. Design maps are presented for all lattice structures processed and tested herein, to demonstrate their relative merits. Moreover, a two-step FEA was executed on a chosen array of lattices to thoroughly investigate the extensive design possibilities, utilising the elastic-plastic, Drucker-Prager, and concrete damage plasticity material models for PlasGray, PA12, and VeroWhite, respectively, with calibration based on experimental results. The results highlight that the tailored design of Gyroid lattices enabled by AM positions them as promising candidates for lightweight energy-absorbing applications.

© 2023 The Authors. Published by Elsevier B.V. This is an open access article under the CC BY license (<http://creativecommons.org/licenses/by/4.0/>).

* Corresponding author. Materials & Manufacturing Research Group, James Watt School of Engineering, University of Glasgow, Glasgow G12 8QQ, UK.

E-mail address: msv.kumar@glasgow.ac.uk (S. Kumar).

<https://doi.org/10.1016/j.jmrt.2023.09.061>

2238-7854/© 2023 The Authors. Published by Elsevier B.V. This is an open access article under the CC BY license (<http://creativecommons.org/licenses/by/4.0/>).

1. Introduction

Foams are naturally occurring or man-made cellular materials with a stochastic arrangement of pores. They are widely used for lightweight structures. By organising pores in an orderly fashion into solids, periodic cellular architectures, also known as lattices capable of exhibiting excellent mass-specific properties such as high specific stiffness and strength can be achieved [1–4]. They are optimised at the unit cell (representative element) level, based on parameters including the relative density (the volume fraction of the solid in the cellular material, $\bar{\rho} = \rho/\rho_s$, where ρ is the density of the cellular material and ρ_s is the density of the solid material with which the cellular structure is made), pore size, and pore morphology for a given choice of material [5]. Furthermore, such architectural parameters can be controlled to tune their deformation patterns and mitigate certain failure modes [6–8]. These lattices are extensively used for energy absorbing structures such as protective devices, packaging and crash-resistant structures [9,10]. Therefore, a nearly constant compressive stress plateau is required, to maximise the energy absorption. Besides absorbing a certain amount of energy, the transmitted stress should be below a certain level to prevent damage to the protected device [11].

Lattice structures comprising macroscale pores exhibit strong coupling between the relative density and the macroscopic properties such as strength and stiffness. Such coupling can be tuned to a certain extent by controlling the porous architecture i.e., by creating repeating building blocks at the micron length scale and organising them in a periodic and systematic manner. Interestingly, this usual coupling can be decoupled for nano-architected lattices where the benefit from the structural size-effect is harnessed. Such architected lattices are referred to as metamaterials. There are many reports on the superior mechanical properties of mechanical metamaterials [12–15]. These metamaterials consist of structural ligaments in the form of trusses, shells, or plates, and they have the capacity to endure substantial compressive strains. Recent advances in micro- and nano-fabrication technologies enable the fabrication of lattices with finer geometric features ranging from submicron up to millimetre scale [16,17].

With additive manufacturing (AM), also known as three-dimensional (3D) printing, it is firstly possible to manufacture highly complex lattice structures across length scales, using polymers, ceramics, metals or composites [18–21]. Unlike traditional manufacturing methods such as grinding or milling which are subtractive, AM is not based on the removal of material to form a finished object [22]. While there are several different methods of AM, they all share the common principle of adding layers in various ways to achieve a desired geometry. The primary techniques include filament-based fused filament fabrication (FFF), powder-based selective laser sintering (SLS) [23], selective laser melting (SLM), along with liquid resin-based methods like inkjet printing, stereolithography (SLA), or digital light processing (DLP) [24–26]. Each process has its own advantages and disadvantages and

can process different families of materials. The vast design possibilities of lattices can be explored by varying the choice of the base material, the unit cell geometry, and the relative density [27].

Exceptional mass-specific strength, stiffness and energy absorption characteristics of AM-enabled lightweight lattice structures have been widely reported. Song et al. [15] report improved mechanical properties and specific energy absorption of octet-truss cellular materials made using photosensitive resin via SLA under compressive loading and demonstrated that they recover up to 30% strain upon unloading. Zheng et al. [1] reported exceptional mechanical properties of micro-architected cellular structures processed via the micro-stereolithography AM technique, across a wide range of relative densities, using polymer, metal and ceramic. Tancogne-Dejean [28] investigated plate-lattices - an emerging class of low-density metamaterials, enabled by direct laser writing and demonstrated that they exhibit nearly isotropic stiffness properties. Ye et al. [29] reported stretching-dominated nature-inspired ultra-low-density tube-in-tube structures, exhibiting near-ideal linear scaling between stiffness and density. Bauer et al. [30] in their work on AM-enabled ceramic micro-truss lattice structures observed and characterised size-dependent strengthening of the alumina shell-based lattices. Using 3D laser lithography, they produced composite lattices and demonstrated excellent size-dependent strength below the densities of 1000 kg/m³. In their study, Gu and Greer [31] fabricated Cu Octet lattices and demonstrated that these structures surpass the yield strength of the bulk materials due to size-effect. Maskery et al. [32] performed a study on Si10–Mg double gyroid lattices for energy absorbing applications, demonstrating the possibility of reducing brittle failure and enhancing strain tolerance through heat treatment, significantly improving the energy absorption capabilities. Andrew et al. [33] fabricated tailored honeycombs via DLP and showed both enhanced impact resistance and energy absorption up to 250% compared to regular honeycomb lattices.

In this study, three different printing techniques and materials were employed to fabricate a selected set of architected lattices. First, a series of lattice structures with very fine microscale features were 3D printed via the DLP technique, using PlasGray™ - a photosensitive resin. Subsequently, a second set of lattice structures was fabricated via SLS using PA12 powder feedstock and finally Material Jetting (MJ) 3D printing was employed to fabricate lattice structures using VeroWhite photo-resin. The effect of relative density on mechanical properties, such as Young's modulus, strength, and energy absorption, was investigated for different unit cell topologies under quasi-static compressive loading. While most of the extant works focused on the behaviour of lattice structures with specific unit cell topologies in the context of a particular material or printing technique, only a few studies thus far investigated and compared the mechanical response and energy absorption efficiency of a variety of lattice structures created using different printing techniques and materials [4,34]. In the present work, we first carry out an extensive experimental campaign to identify the best-performing lattice

structures and their architectural parameters from a set of truss-, shell- and plate-based lattice structures. We determine the effect of the relative density on the macroscopic stress-strain response under uniaxial quasi-static compression. While the plate-based simple cubic (SC) lattice structure shows the best performance in terms of stiffness and strength, the shell-based Gyroid structure outperforms others in terms of energy absorption efficiency, especially at lower relative densities. Based on the measured macroscopic and microscopic tensile and compressive stress-strain data of the polymeric materials explored, elastic-plastic, Drucker-Prager and Concrete damage plasticity models' constitutive parameters were identified for finite element analysis (FEA). Two-step FE simulations of lattices under quasi-static compression were then performed up to the densification to assess the measured energy-absorbing characteristics. By utilising three different material models, we accurately captured the mechanical response of lattices made of three different materials explored in this study. The Drucker-Prager model accounts for

the mismatch in yield stress between tension and compression, as observed for PA12 and the concrete damage plasticity model captures the pronounced softening behaviour of Verowhite. Size-dependent mechanical properties variation is observed for micro- and macroscale ligaments in the lattices made from photopolymers and is reported.

2. Materials and methods

2.1. Materials and additive manufacturing processes

Lattice structures with micro- and mesoscale architectures were fabricated using three different materials and additive manufacturing processes.

2.1.1. Material jetting (MJ)

A first set of lattice structures was printed using the Object 260 Connex industrial Material Jetting (MJ) printer (Stratasys, Ltd.)

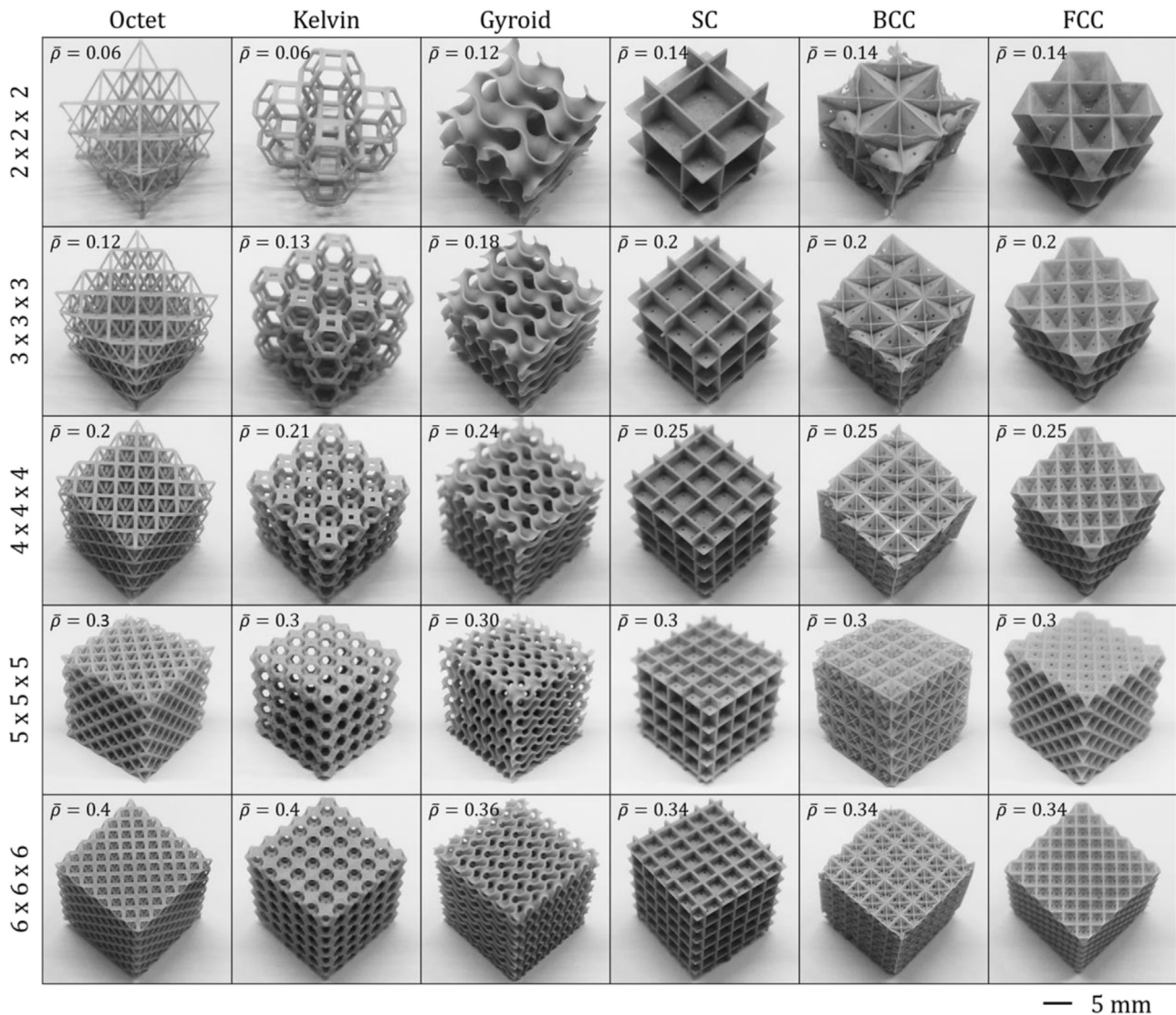


Fig. 1 – Different 3D printed lattice structures of size $20 \times 20 \times 20 \text{ mm}^3$ using PlasGray™ with increasing relative density (top to bottom).

using VeroWhite - an opaque photosensitive resin, that is solidified layer-by-layer during the printing process using ultraviolet (UV) light to produce a 3D printed geometry. A support material (SUP705) ensures the correct placement of the resin during photo-polymerisation and is removed after printing. Compared to standard engineering plastics such as acrylonitrile butadiene styrene (ABS), VeroWhite is stronger and stiffer both under tensile and compressive loads [35].

2.1.2. Selective laser sintering (SLS)

A second set of lattice structures was printed via selective laser sintering (SLS) using a SnowWhite 3D printer (Sharebot S. r.l.), a process in which polymer powder is sintered using a laser heat source, selectively binding the material to form a solid object. The printing process can be divided into three phases: preheating, building and cooling [36]. First, the powder bed or environment is heated and maintained at a high temperature. Second, the powder is placed on to the build plate layer-by-layer using a coating blade, and the thermoplastic powder particles are selectively fused using a high-power CO₂ laser based on the sliced computer model. Once the build is complete, the chamber is slowly cooled to prevent warping and finally, the remaining powder, which acted as a support, can be removed. The polymer powder used in this study is commercial DuraForm polyamide 12 (PA12) from 3D Systems Corporation [37], which has been artificially aged to achieve uniform properties over multiple prints, while allowing the printing parameters to be kept constant [38]. No additional support material is required, as the surrounding powder in the print bed supports the structure.

2.1.3. Digital light processing (DLP)

Finally, a series of microscale lattice structures were printed using the PlasGray photopolymer on an Asiga Pro2 (Asiga) high-resolution DLP printer. In DLP, an object is created by selectively curing a photosensitive polymer resin, located in a container with a transparent bottom over the UV light source, onto which the sliced computer aided design (CAD) model is projected layer-by-layer. The build platform moves upwards during the printing process to make room for the next layers. After printing, the structures were removed from the build

platform, washed with isopropyl alcohol and cured for an additional 5 min in an Asiga flash UV chamber.

2.2. Lattice architectures

In total, six different lattice designs were considered. Firstly, a family of elementary plate-lattices reported by Tancogne-Dejean et al. [28] was investigated including the stretching-dominated simple cubic (SC), the bending-dominated body centred cubic (BCC), and the face centred cubic (FCC) architectures. Secondly, the stretch-dominated octet-truss (O) [39] and the bending-dominated kelvin-truss (K) geometries were explored [1]. Finally, the stretch-dominated shell-based minimal surface architecture (see Eq. (1)), namely Gyroid (G) lattice generated using MATLAB [40,41] was studied:







$$\cos\left(\frac{2\pi}{L}x\right)\sin\left(\frac{2\pi}{L}y\right) + \cos\left(\frac{2\pi}{L}y\right)\sin\left(\frac{2\pi}{L}z\right) + \cos\left(\frac{2\pi}{L}z\right)\sin\left(\frac{2\pi}{L}x\right) = 0 \tag{1}$$

where L is the unit cell size. The function describes a two-dimensional surface, which was thickened to create a shell of specific thickness.

The unit cell size, L, and wall thickness, t, or strut diameter, d, were separately chosen for each set of lattices considering the resolution of the three different 3D printers employed. For achieving the highest resolution and smallest geometric features of the lattices, the DLP manufacturing method was used. DLP enables features that are thinner and smaller than those produced by SLS and MJ additive manufacturing methods. However, while the wall thickness and strut diameter for the DLP prints are in the micron length scale (<1 mm), the topologies processed via MJ AM using VeroWhite exceed this scale for some cases.

For the lattice structures printed via DLP using PlasGray, the overall dimensions were set to 20 × 20 × 20 mm³. Keeping the wall thickness and strut diameters constant, the relative density was changed by varying the unit cell size, L. Accordingly, the number of unit cells is in the range of 2 × 2 × 2 for low relative density lattices and is up to 6 × 6 × 6 for high relative density lattices (Fig. 1). This results in a unit cell size,

Table 1 – Architectural parameters for different micro-architected lattices fabricated via DLP AM using PlasGray. Designed unit cell size, L, designed relative density, $\bar{\rho}$, designed strut diameter, d, designed plate thickness, t and measured mass, m, are summarised.

PlasGray™		Octet	Kelvin	Gyroid	SC	BCC	FCC						
													
Conf.	L [mm]	d = 694 μm		d = 999 μm		t = 394 μm		t = 479 μm		t = 170 μm		t = 213 μm	
		$\bar{\rho}$	m [g]	$\bar{\rho}$	m [g]	$\bar{\rho}$	m [g]	$\bar{\rho}$	m [g]	$\bar{\rho}$	m [g]	$\bar{\rho}$	m [g]
2 × 2 × 2	10	0.06	0.43	0.06	0.48	0.12	0.96	0.14	1.28	0.14	1.43	0.14	2.49
3 × 3 × 3	6.67	0.12	1.92	0.13	1.04	0.18	1.44	0.2	1.81	0.2	1.58	0.2	3.21
4 × 4 × 4	5	0.2	1.59	0.21	1.75	0.24	2.02	0.25	2.38	0.25	1.65	0.25	2.87
5 × 5 × 5	4	0.3	2.43	0.3	2.55	0.3	2.38	0.3	2.69	0.3	1.69	0.3	2.00
6 × 6 × 6	3.33	0.4	3.39	0.4	3.46	0.36	3.35	0.34	3.01	0.34	1.68	0.34	3.35

of 3.33 mm up to 10 mm, with a relative density of 0.06–0.4 for truss lattice structures, and 0.12 to 0.34 for plate-lattice structures, respectively (Table 1).

While all six structures were printed by DLP using PlasGray for a range of relative densities (see Table 1), only four structures were printed via SLS using PA12 and MJ using VeroWhite for a configuration of $4 \times 4 \times 3$ unit cells with a unit cell size of 7 mm and a relative density of $\bar{\rho} = 0.23$ (see, Table S1, Table S2 in Supporting Information (SI) and Fig. 2), to keep the experimental effort within a reasonable limit. However, the FCC and BCC plate-lattice structures would have resulted in such thin features for the chosen relative density and unit cell size that they simply could not be printed using SLS and MJ methods. An additional set of Gyroid structures was produced using the MJ printer, varying the relative density by changing the unit cell size while keeping the overall dimensions and wall thickness of the structure constant (Table S2). These different approaches to varying the relative density ensure that we work at the limits of printers' resolution and capabilities.

Holes with a radius of 250 μm were added at the centre of each bounding surface for the plate-lattice structures to allow for the removal of residual resin after the DLP printing process using isopropyl alcohol. For the SLS and MJ prints, the SC structures were modified accordingly with holes having a radius of 350 μm to remove the remaining powder and support material. Measurement of the actual mass of the printed PlasGray lattices after removal of the residual resin showed (Table 1) entrapment of small amount of resin within the FCC structure increasing their weight although such entrapped resin has no significant influence mechanically and hence on the stiffness and strength of lattices. As it does affect the weight, the lattices need to be cleaned and optimally dried after printing for further applications.

The relative density required for modelling purposes for each of the lattice architecture presented herein can be expressed as:

$$\bar{\rho}_O = \left(12\sqrt{2}\pi Lr^2 - 36\sqrt{2}\pi r^3\right) / L^3 \quad (2)$$

$$\bar{\rho}_K = \left(6\sqrt{2}\pi Lr^2 - \frac{96}{5}\pi r^3\right) / L^3 \quad (3)$$

$$\bar{\rho}_{SC} = (3L^2t - 3Lt^2 + t^3) / L^3 \quad (4)$$

$$\bar{\rho}_{BCC} = \left(6\sqrt{2}L^2t - 24Lt^2 + 16\sqrt{2}t^3\right) / L^3 \quad (5)$$

$$\bar{\rho}_{FCC} = \left(\left(4\sqrt{3} - \frac{3}{5}\right)L^2t - \left(6 - \frac{2}{5}\sqrt{3}\right)Lt^2 + 2\sqrt{3}t^3\right) / L^3 \quad (6)$$

where L is the unit cell size, t is the wall thickness and r is the strut radius. The subscripts O, K, SC, BCC, and FCC refer to the Octet, Kelvin, simple cubic, body centred cubic, and face centred cubic lattice geometries, respectively. The volume and relative density of the Gyroid structure were calculated from the CAD geometry using MATLAB.

2.3. Experimental procedure

Uniaxial quasi-static compression tests were performed in accordance with ASTM D1621 [42] - the standard test method for examining the compressive properties of rigid cellular plastics, to analyse the energy absorption properties of the lattice structures. Compression tests were performed using a Zwick/Roell Z005 Universal Testing Machine (UTM) with a 2.5 kN load cell at a rate of 5 mm/min. For lattices with higher relative densities, where 2.5 kN was insufficient to capture the compressive force to densification, an Instron 5569 UTM fitted with a 50 kN load cell was used. The force-displacement response was recorded and the mechanical properties such as Young's modulus, strength and energy absorption were calculated for each cellular structure. Using the slope of the

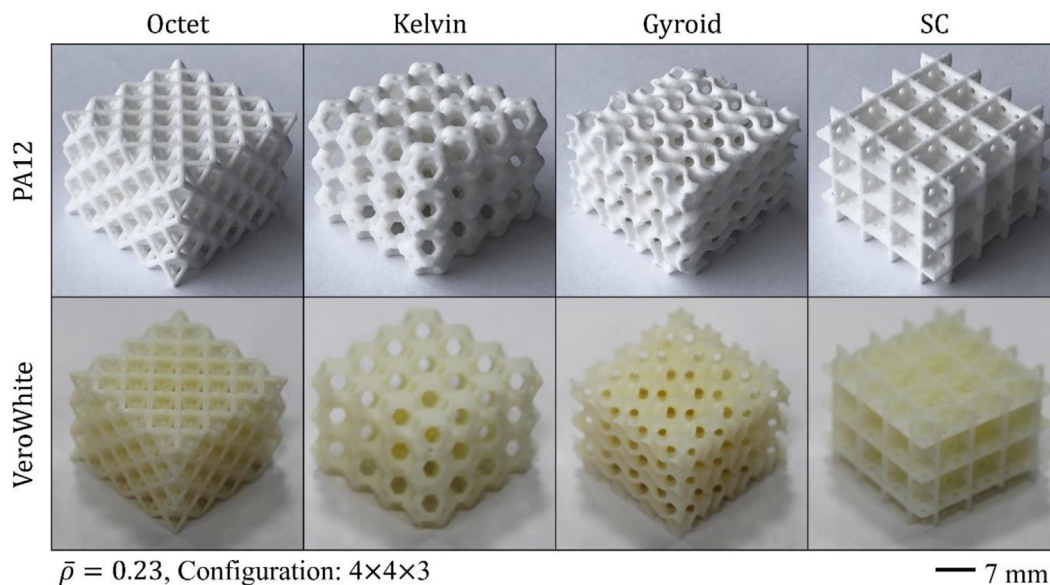


Fig. 2 – Lattice structures comprising $4 \times 4 \times 3$ unit cells with a relative density of 0.23 processed by SLS using PA12 (top row) and by MJ AM using VeroWhite (bottom row).

stress-strain response, the Young's modulus E , was calculated within the elastic range using:

$$E = \frac{\sigma}{\epsilon} = \frac{F/A}{\Delta l/l_0} \quad (7)$$

where F is the applied force, A is the cross section of the lattice structure, Δl is the change in length and l_0 is the initial height of the specimens. The strength of the structures corresponds to the initial peak of the stress-strain curve. The energy absorption, W , is calculated by integrating the area under the stress-strain curve from zero up to the densification strain, ϵ_d , and is the energy absorbed by the lattice structure due to mechanical deformation per unit volume prior to densification.

$$W = \int_0^{\epsilon_d} \sigma(\epsilon) d\epsilon \quad (8)$$

The densification strain is defined as the onset strain of densification. Here, the strain at which densification begins is determined by the point at which the tangents to the stress plateau region and the densification region intersect as reported elsewhere [43]. The energy absorption efficiency is given by

$$\eta = \frac{1}{\sigma_p} \int_0^{\epsilon_d} \sigma(\epsilon) d\epsilon \quad (9)$$

where σ_p is the peak stress produced prior to densification. η is the ratio of area under the stress-strain curve to that of an ideal energy absorbing material with the maximum stress σ_p and the maximum theoretical strain $\epsilon = 1$. An ideal structure exhibits a rigid behaviour with no elastic regime until the compressive strength of the energy absorber is reached, at which it begins to collapse uniformly up to 100% strain. The efficiency of the ideal energy absorber increases linearly with the strain.

2.4. Finite element modelling

The geometric models of the lattice structures were created using SolidWorks and imported into Abaqus/explicit for performing nonlinear FEA. Elastic-plastic (EP), Drucker-Prager (DP) and Concrete damage plasticity (CDP) material models were considered for PlasGray, PA12, and VeroWhite, respectively. The different choice of material models is intended to accurately capture the unique mechanical response of each of these materials.

As an extension of the Mohr-Coulomb model, the DP model finds widespread use in simulating the behaviour of materials capable of undergoing both elastic and plastic deformation. The DP model possesses a unique capability to accurately represent materials with compressive yield strengths surpassing their tensile yield strengths, as often observed in composites or polymers and here for PA12. During small deformation until the material reaches its yield point, the model assumes linear elasticity, where stress is directly proportional to strain. The transition from elastic to plastic behaviour is determined by a yield criterion, which hinges on the shape of a yield surface in the

meridional plane. In Abaqus/Explicit, this surface assumes a linear shape. The yield criterion relies on the deviatoric stress (stress deviation from hydrostatic pressure) and the internal friction angle of the material to match yield values in triaxial tension and compression, which may differ. Once the material has yielded, the plastic flow rule governs its plastic deformation. The plastic flow corresponds to an equivalent plastic strain based on a rule rooted in the deviatoric stress state. The DP model accommodates isotropic hardening. This behaviour is controlled by parameters like the dilation angle. Detailed description of this model can be found in the Abaqus manual [44].

To calibrate the DP material model for PA12, the Young's modulus of the bulk material was determined as 1061 MPa, and the Poisson's ratio as 0.39 based on macroscopic tensile response of bulk material (Fig. 3). The density was found to be 1.01 g/cm³. The angle of friction and the angle of dilation were both set to 20°. Dilatancy phenomenon was disregarded since ductile deformation was assumed to be associated solely with shear yielding, resulting in the angle of dilation being equal to the angle of friction. To account for failure, a ductile damage model was utilised, with a fracture strain of 1 and 0.15 for a stress triaxiality of -0.33 and 0.33, respectively. The damage evolution was assumed to follow linear softening behaviour and was considered to be strain rate independent.

For PlasGray, an EP material model was employed. The constitutive parameters of the material model were evaluated using the stress-strain data obtained from tensile tests performed on microscale bulk specimens. Curing related, size-dependent material property variations were observed even at macroscale, and lattice structures in this study were exclusively manufactured at micron length scale. The linear elastic regime is characterised by the Young's modulus and Poisson's ratio and they were experimentally determined to be 209 MPa, and 0.47 for PlasGray, respectively. At higher strain levels, after yielding, PlasGray exhibits non-linear plastic deformation. This data is implemented into Abaqus in the form of true stress as a function of plastic strain obtained from tensile tests performed on the bulk material. The strain increment and the true strain respectively, are: $d\epsilon = dl/l_0$ and $\epsilon = \int_{l_0}^l dl/l$, where l is the instantaneous length and l_0 is the

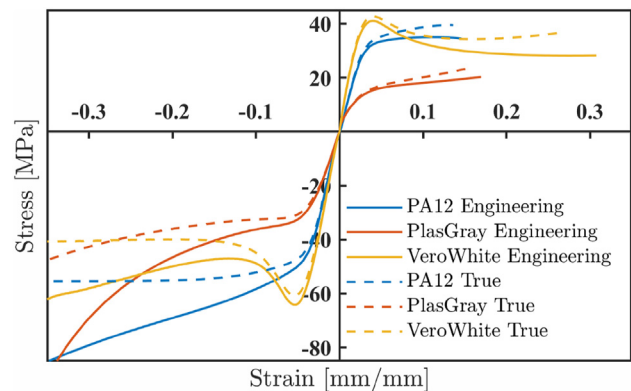


Fig. 3 – Measured engineering and true stress-strain responses of PA12, PlasGray and VeroWhite materials obtained from macroscopic tensile and compression tests.

original length. The stress conjugate to the true strain is the true stress and is given by $\sigma = F/A$ with F being the force applied on the specimen, and A the instantaneous cross-section of the specimen. To define plastic strain in Abaqus, the experimentally evaluated stress-strain response (engineering stress-strain) must be converted to the true stress-strain response as follows:

$$\varepsilon_t = \ln(1 + \varepsilon_{\text{eng}}) \quad (10)$$

$$\sigma_t = \sigma_{\text{eng}} (1 + \varepsilon_{\text{eng}}) \quad (11)$$

To account for failure and crack initiation, a ductile damage model was implemented. Fracture strains were assigned values of 1 and 0.35 for stress triaxialities of -0.33 and 0.33 , respectively. The stress triaxiality is a measure of the relative magnitudes of the three principal stresses in a material and helps characterise the stress state to assess the likelihood of ductile fracture. It is defined as the ratio of the hydrostatic stress to the equivalent von Mises stress [45]. The displacement at failure, which refers to the displacement level at which the material is considered to have failed completely, having lost all load-carrying capacity, was defined as 0.03 mm. The element deletion functionality was activated to remove elements that experienced failure during the deformation process. Further information on the elastic-plastic material model is provided in the supporting information.

The VeroWhite material's constitutive response was simulated using the damage-plasticity model developed by Lubliner et al. [46] for reinforced concrete. To calibrate the model, data from Fig. 3, depicting uniaxial tension and compression stress versus strain was utilised, along with plasticity parameters shown in Table S4. A non-associated flow rule was selected with a dilation angle set to 40° to mimic the softening behaviour in tension and compression. The eccentricity is a parameter used to represent the off-centre loading of a specimen. It is the distance between the centre of the element and the line of action of the applied load. Eccentric loading can significantly affect the behaviour of the material in terms of its deformation and cracking patterns. fb_0/fc_0 are parameters used to define the ratio of uniaxial tensile strength (fb_0) to the initial uniaxial compressive strength (fc_0). K is the softening parameter associated with the post-peak softening of the material under both tension and compression. Damage was incorporated in compression utilising damage parameters as a function of inelastic strain, as well as in tension, where the damage parameters are as a function of cracking strain. The damage variables,

both in tension and compression, vary from 0 (undamaged state) to 1 (complete failure), as the material undergoes tension or compression, respectively. The evolution of these damage variables is governed by specific damage evolution laws and criteria, which are defined in the material model [47]. Prior to plastic deformation, the VeroWhite material exhibited isotropic and linear elastic behaviour with Young's modulus of 1.5 GPa and Poisson's ratio of 0.35 . For a detailed constitutive description, please see the Supporting Information of our previous publication [19].

Irrespective of the material model, C3D10 M tetrahedral solid elements were chosen to mesh the geometries of the Octet and Kelvin, SC, BCC and FCC lattice structures. The Gyroid structure was modelled using S4 four-node shell elements. The global seed size was set between 0.18 and 0.4 mm, depending on the geometry and detail required, to eliminate mesh density dependent inaccuracies in the FE results. Mass scaling was introduced with a target time increment of 1^{-5} to increase the computational speed without compromising the accuracy of the results. The structures were placed between two parallel rigid platens, assuming a tangential friction coefficient of 0.2 . The lower platen was fixed (all degrees of freedom were set to zero), as shown in Fig. S1, while the upper platen moved downwards at a constant speed to compress the specimen to full densification. A general contact algorithm of Abaqus explicit was applied to avoid penetration of the contact surfaces into each other during the compression test. The displacement and the corresponding reaction force on the top plate were recorded. For selected structures prone to buckling, a two-step analysis was performed. In the first step, a buckling analysis was performed to determine the eigenmodes of these structures. Prior to performing the explicit analysis, imperfections based on the first three eigenmodes were applied to the geometry. The two-stage analysis ensures that the initial stiffness is reduced to reflect a realistic environment, considering early failure due to buckling. The accuracy of the material models employed was verified by simulating the bulk tensile and compressive response of the parent materials, with good (VeroWhite) to excellent (PlasGray, PA12) agreement between FE and experimental results (Fig. 4).

3. Results and discussion

Quasi-static compression tests on lattice structures were carried out for lattices fabricated using PlasGray, PA12 and

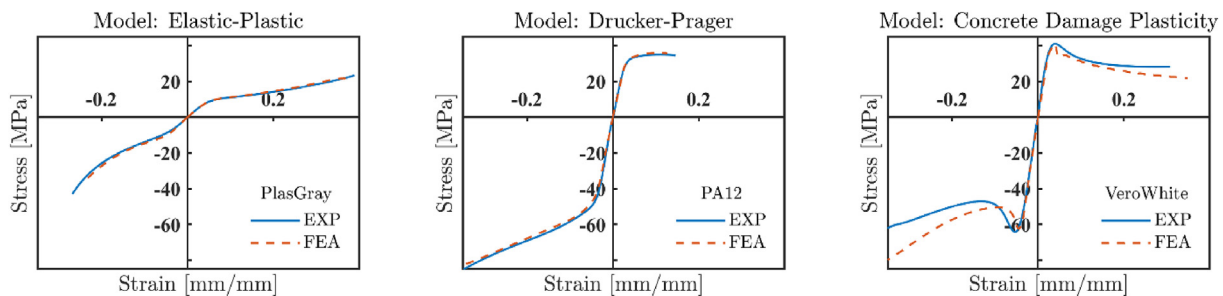


Fig. 4 – Comparison of measured tensile and compression stress-strain responses of the parent materials PlasGray, PA12 and VeroWhite with those obtained from the FEA using EP, DP, and CDP material models respectively.

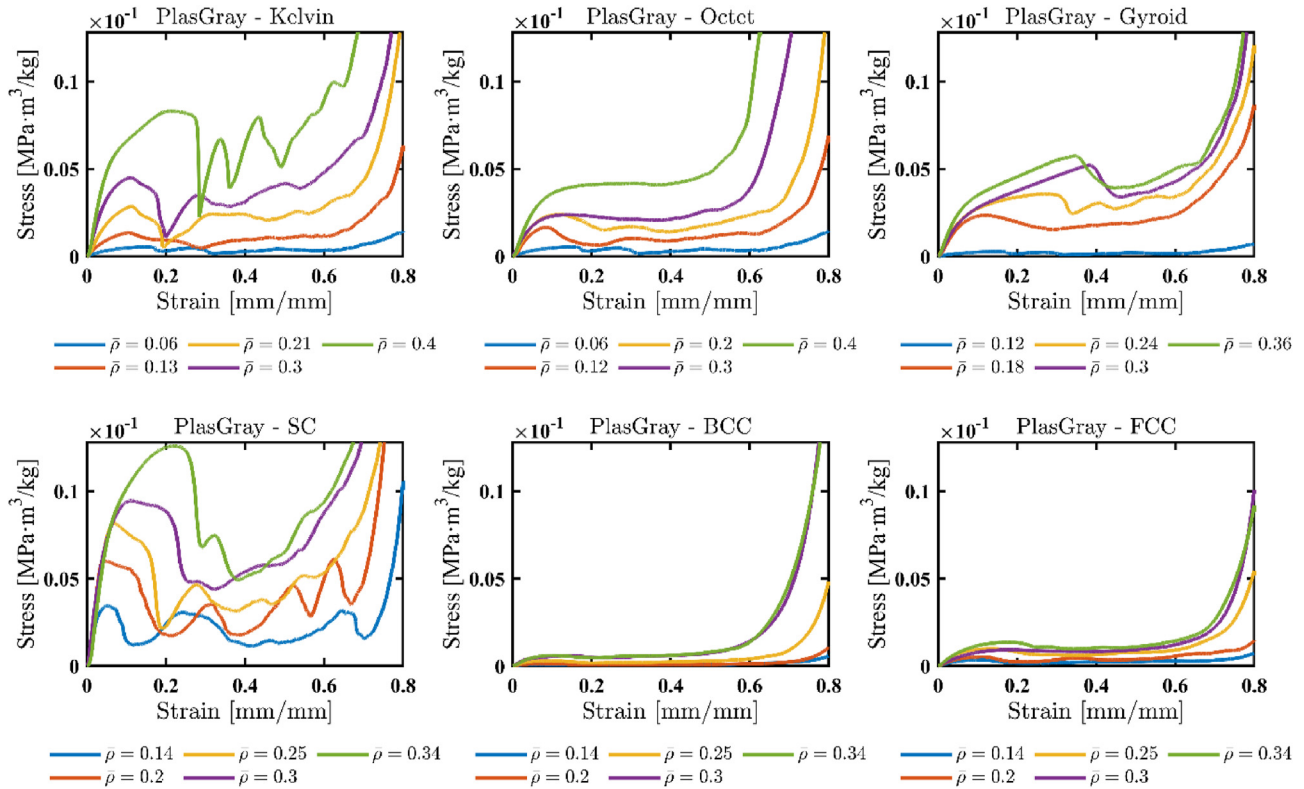


Fig. 5 – Measured engineering stress-strain response of different PlasGray lattice structures for different choices of relative density under quasi-static compression.

VeroWhite as for the configurations summarised in Table 1, Table S1 and Table S2, respectively. The corresponding mass-specific macroscopic engineering stress as a function of the uniaxial engineering strain are shown in Fig. 5 and Fig. 6a–c.

All lattices made of PlasGray show an almost linear stress-strain response within the elastic regime up to ~5% strain, after which the material yields and plastic deformation begins, slowing down the increase in stress and attains a maximum between 10 and 20% strain (Fig. 5). This is followed by the plateau region where the lattices exhibit either uniform deformation or a brittle, layer-by-layer failure until the densification onset somewhere between 50% and 80% strain depending on the relative density. SC and Kelvin structures show a significant drop in strength after an initial peak between 10 and 20% strain, indicating brittle failure of ligaments with layers collapsing on each other, or as observed in some cases, global brittle failure due to fracture/failure throughout the structure, for e.g., see Kelvin lattice with $\bar{\rho} = 0.3$ (see video SV1 in supplementary information). The Octet structure shows a stress plateau up to densification for relative densities of 0.3 and above, where no local failure was observed prior to densification, which is ideal for energy absorption applications. At lower relative densities it shows an unstable deformation pattern caused by buckling of the ligaments, causing layers to collapse one by one. The engineering stress in the Gyroid structure increases continuously after yielding at a slower rate of up to about 40% strain for structures of $\bar{\rho} = 0.24$ and above, which is a unique response among the structures examined. After a slight decrease in stress,

densification begins at higher strains than the competing structures, indicating that more energy can be absorbed prior to densification. Even at lower relative densities, the Gyroid structures show a large stress plateau region ideal for energy absorption applications. The FCC and BCC structures show comparatively low stress peaks and a plateau region with uniform deformation up to densification.

It can be observed that the SC structure outperforms all other structures in terms of Young's modulus, strength, and energy absorption, over a range of relative densities considered here (see, Fig. 7 and Table 2). The Young's modulus, strength and the energy absorption vary from 26 MPa to 80 MPa, 0.6 MPa–5 MPa and 0.3 MJ/m³ to 2.25 MJ/m³ respectively when the relative density increases from $\bar{\rho} = 0.14$ to 0.34. In accordance with Eqs. (1) and (2) in the supporting information, the scaling relations $\bar{E} \propto \bar{\rho}^{1.02}$ and $\bar{\sigma}_y \propto \bar{\rho}^{1.43}$ were determined and they indicate a stretching-dominated behaviour. The exponents n and m and the scaling constants C_1 and C_2 were determined by power law curve fitting using the curve fitting tool of MATLAB (Mathworks Inc., USA).

For the Kelvin lattice structures, the scaling relationships are $\bar{E} \propto \bar{\rho}^{2.42}$ and $\bar{\sigma}_y \propto \bar{\rho}^{2.42}$, indicating a clear bending-dominated behaviour. For the Gyroid lattice structures, $\bar{E} \propto \bar{\rho}^{-1.7}$ and $\bar{\sigma}_y \propto \bar{\rho}^{-1.65}$ signal a bending-dominated behaviour but to a lower degree than the Kelvin lattice structure. The Octet lattice structures demonstrate comparable performance to Gyroid and Kelvin structures for low relative densities, but they are unable to compete at relative densities above 0.2.

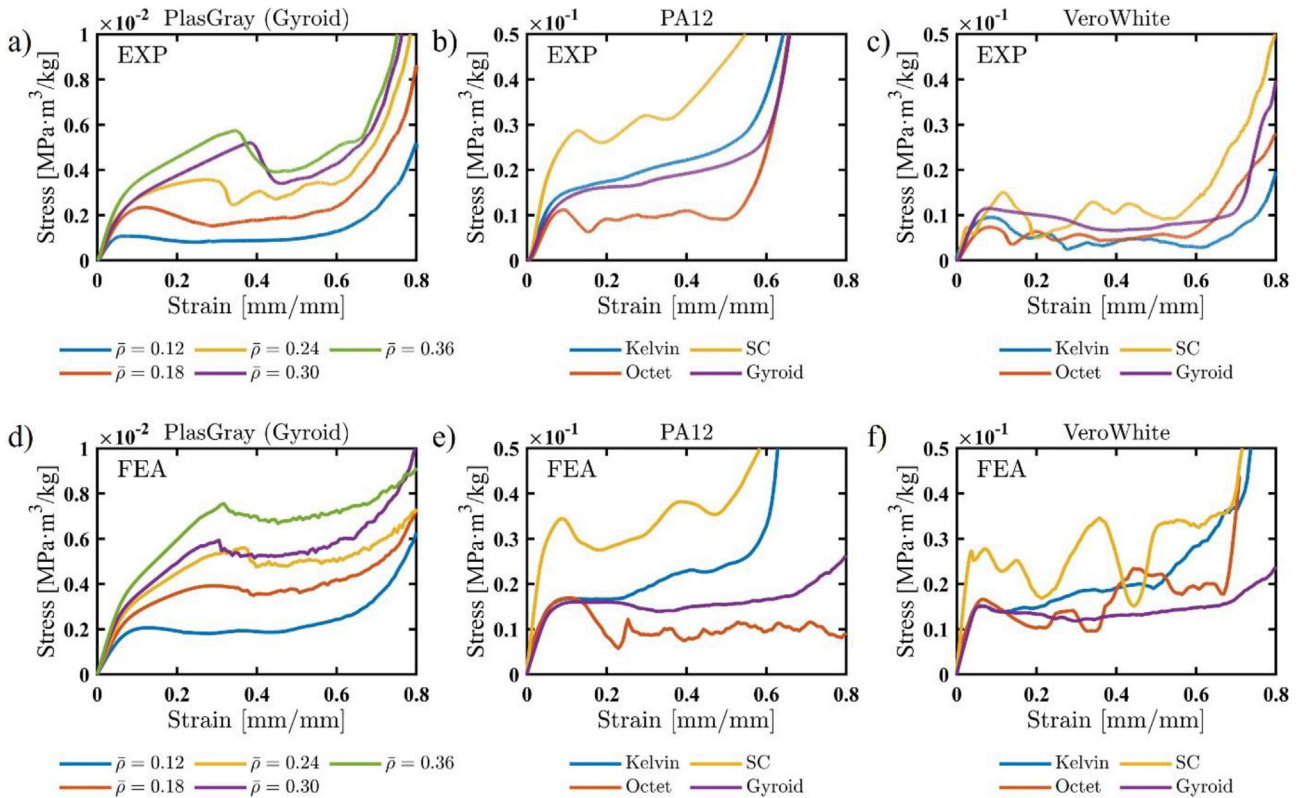


Fig. 6 – Measured, mass-specific engineering stress-strain responses of a) Gyroid lattices for various relative densities, manufactured by PlasGray; b) PA12 ($4 \times 4 \times 3$ unit cells) with a relative density of 0.23; and c) VeroWhite lattice structures ($4 \times 4 \times 3$ unit cells) with a relative density of 0.23, all under quasi-static compression. Figures (d–f) showcase the corresponding engineering stress-strain responses obtained from FEA utilising their respective material models.

With $\bar{E} \propto \bar{\rho}^{1.5}$ and $\bar{\sigma}_y \propto \bar{\rho}^{1.54}$, Octet structures exhibited stretching-dominance, although to a lesser extent than the SC lattice structures. This may be attributed to the buckling of struts at lower densities, a phenomenon also reported by Tancogne-Dejean et al. [27] for relative densities below 0.3.

The FCC and BCC lattice structures underperform and fall short of expectations due to printing-induced defects associated with their thin feature sizes (Fig. 1). Consequently, they do not exhibit adequate stiffness and do not

absorb significant amounts of energy. Further observations revealed that the wall thicknesses of 213 μm and 170 μm for FCC and BCC structures, respectively, were insufficient for providing the desired stiffness and energy absorption for the choice of materials and AM techniques employed. The weight measurement of the BCC structure further confirms that, at higher densities, it weighs up to 50% less than designed weight, highlighting the limitations of the 3D printer's resolution in accurately reproducing the model.

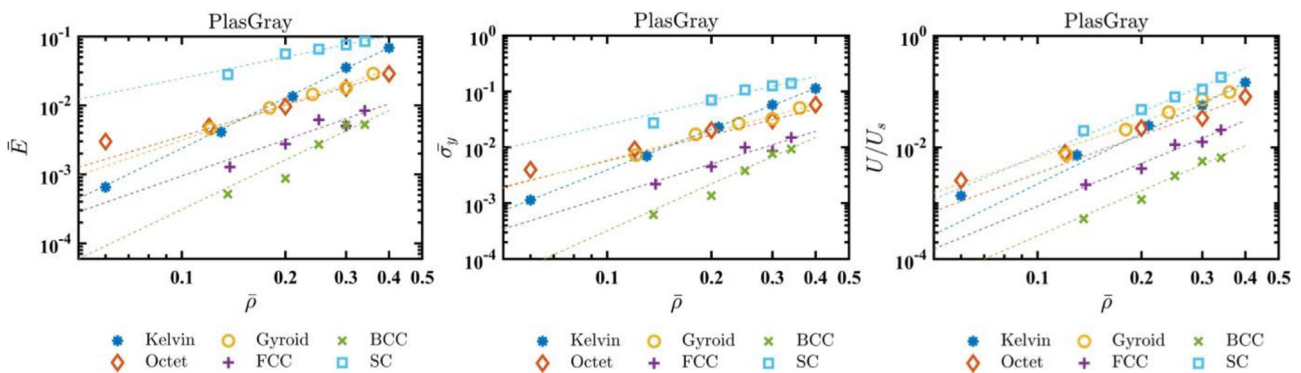


Fig. 7 – Normalised Young's modulus, yield strength and energy absorption of PlasGray lattice structures measured for different relative densities under quasi-static compression.

Table 2 – Summary of mechanical properties and scaling constants measured for a variety of lattice structures printed using PlasGray via DLP technique.

Configuration	$\bar{\rho}$	E [MPa]	σ [MPa]	W [kJ/m ³]	η	C ₁	n	C ₂	m
Octet	2 × 2 × 2	0.06	2.97	0.08	32.1	0.40			
	3 × 3 × 3	0.12	5.47	0.23	100.1	0.43			
	4 × 4 × 4	0.2	11.14	0.56	277.1	0.49	0.11	1.5	0.2
	5 × 5 × 5	0.3	16.85	0.84	420.1	0.50			1.54
	6 × 6 × 6	0.4	32.50	1.93	1012.4	0.52			
Kelvin	2 × 2 × 2	0.06	0.61	0.04	17.1	0.45			
	3 × 3 × 3	0.13	3.87	0.21	90.8	0.44			
	4 × 4 × 4	0.21	12.67	0.71	306.7	0.43	0.63	2.42	1.04
	5 × 5 × 5	0.3	33.17	1.59	712.1	0.45			
	6 × 6 × 6	0.4	64.29	3.91	1816.8	0.47			
Gyroid	2 × 2 × 2	0.12	4.32	0.15	93.5	0.61			
	3 × 3 × 3	0.18	8.65	0.50	261.9	0.53			
	4 × 4 × 4	0.24	13.61	0.96	534.3	0.53	0.16	1.7	0.26
	5 × 5 × 5	0.3	16.85	1.33	906.2	0.49			
	6 × 6 × 6	0.36	27.18	1.93	1220.7	0.50			
SC	2 × 2 × 2	0.14	26.32	0.55	249.6	0.45			
	3 × 3 × 3	0.2	52.39	1.42	596.3	0.42			
	4 × 4 × 4	0.25	61.56	2.41	1008.1	0.42	0.26	1.02	0.69
	5 × 5 × 5	0.3	70.64	3.34	1380.9	0.41			
	6 × 6 × 6	0.34	79.68	5.02	2259.6	0.45			
BCC	2 × 2 × 2	0.14	0.49	0.01	6.6	0.48			
	3 × 3 × 3	0.2	0.82	0.03	14.7	0.49			
	4 × 4 × 4	0.25	2.55	0.09	38.8	0.43	0.08	2.38	0.19
	5 × 5 × 5	0.3	4.89	0.21	70.5	0.34			
	6 × 6 × 6	0.34	4.95	0.24	81.8	0.35			
FCC	2 × 2 × 2	0.14	1.20	0.06	26.9	0.48			
	3 × 3 × 3	0.2	2.58	0.13	52.3	0.42			
	4 × 4 × 4	0.25	5.80	0.29	140.5	0.49	0.05	1.74	0.11
	5 × 5 × 5	0.3	4.73	0.33	156.8	0.48			
	6 × 6 × 6	0.34	7.91	0.54	258.6	0.48			

In addition to these observations, the energy absorption efficiency, η , was evaluated using Eq. (9), and the results for different densities and lattice structures are presented in Fig. 8. It shows that the Gyroid structure outperforms all the other lattice structures, particularly at low relative densities where η reaches up to 61%. The Octet structure surpasses the energy absorption efficiency of the Gyroid only for densities

above 350 kg/m³, while displaying the opposite trend – efficiency increases with higher relative densities, showing an increase in efficiency for higher relative densities. This behaviour can be attributed to the Octet structure's unstable performance at low relative densities, where buckling becomes dominant, whereas no buckling was observed for the Gyroid structures or Octet structures at higher relative densities.

The BCC structure exhibits a trend of a decreasing efficiency with increasing density, albeit with 10–15% lower than that of the Gyroid lattice. The Kelvin and SC lattice structures demonstrate nearly constant efficiency of approximately 45% across all densities. The FCC structure follows a linear trend, except for an anomaly observed at a density of 236 kg/m³, where it drops to 42%. This anomaly is likely due to poor printing quality consistently observed for these structures.

As observed for PlasGray, the SC lattice structures fabricated using PA12 via SLS exhibit superior stiffness, strength, and energy absorption (see, Fig. 6b). The stress-strain response displays two minor peaks before reaching early densification at approximately 40% strain, distinguishing it from the other structures. This behaviour can be attributed to the more ductile response of PA12 compared to the relatively brittle response of PlasGray. Following the SC lattice structure, the Kelvin and Gyroid lattice structures exhibit similar responses, with the Kelvin structure being slightly stiffer and stronger. Both structures demonstrate continuously increasing stress (work hardening) after yielding, showcasing

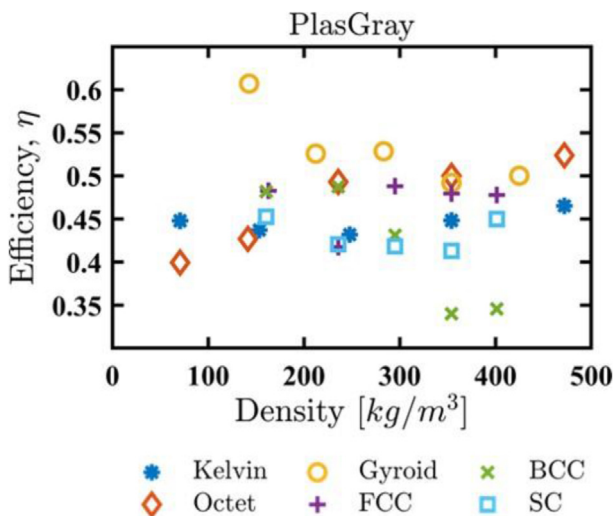


Fig. 8 – Measured energy absorption efficiency of different lattices made of PlasGray as a function of density.

Table 3 – Experiments vs. Numerical: Energy absorption characteristics of different lattice structures with $4 \times 4 \times 3$ unit cell configuration, processed by SLS using PA12 for $\bar{\rho} = 0.23$.

PA12	E [MPa]		σ [MPa]		W [MJ/m ³]		η	
	EXP	FEA	EXP	FEA	EXP	FEA	EXP	FEA
Octet	54.3 ± 11.6	69.4	2.2 ± 0.5	3.9	0.95 ± 0.29	1.9	0.43 ± 0.02	0.50
Kelvin	72.2 ± 23.1	70.3	3.3 ± 1.1	3.9	2 ± 0.45	2.4	0.68 ± 0	0.62
Gyroid	60.3 ± 21.3	63.9	3.1 ± 0.9	3.7	2.01 ± 0.33	2.3	0.68 ± 0.07	0.61
SC	156.7 ± 4.8	156.7	6.9 ± 0.3	8.0	2.98 ± 0.18	3.7	0.51 ± 0.01	0.47

excellent energy absorption capabilities. The ductile material response contributes to a more uniform deformation pattern, particularly noticeable in the Kelvin structure, compared to PlasGray where layer-by-layer failure was observed. In contrast, the Octet structure exhibits the lowest strength at around 10% strain, resulting in the lowest observed energy absorption among all the structures (Table 3). The smaller strut diameter, compared to the Kelvin structure, leads to slightly less uniform plastic deformation and a more brittle response. This manifests in the sequential breaking of struts, particularly in the outer region, until densification occurs.

The stress-strain responses of the VeroWhite lattice structures exhibit less pronounced differences compared to the structures made of other investigated materials (Fig. 6c). Each structure demonstrates an initial peak strength at around 10% strain, followed by oscillating post-yield response resulting from layer-by-layer failure of the struts and plates. Among the VeroWhite structures, only the Gyroid exhibits uniform deformation with a smooth plateau region, achieving an energy absorption efficiency of 53% (Table 4). In contrast to PA12 and PlasGray, VeroWhite displays a pronounced brittle response under compression. Examination of deformation maps reveals that the VeroWhite structures tend to fail layer-by-layer, while the lattice structures made of other materials, especially PA12, exhibit a more uniform deformation and failure pattern. Moreover, tensile and compression tests conducted on bulk samples printed using VeroWhite show softening behaviour after yielding, evidenced by a significant drop in the stress after reaching the maximum value (Fig. 3). This behaviour is reflected in the response of the lattice structures under compression. While the SC lattice structure still outperforms the other structures, its superiority is less pronounced. This is evident from the initial drop in the stress at around 5% strain, where the top half layer of the lattice fails before reaching maximum strength, a phenomenon not observed with the same lattice structure made of other materials investigated herein.

A series of Gyroid structures printed with VeroWhite (Table S2, row 2–6) exhibit a similar trend of decreasing energy

absorption efficiency with increasing density, akin to what was observed for PlasGray. However, the efficiency values for VeroWhite structures are consistently 10–15% lower. While there is an overall increasing trend, the optimal relative density appears to be around 0.23–0.24 (approximately 271 kg/m³), which yields the highest observed efficiency for the VeroWhite lattices, ranging from 41 to 53% (Fig. 9, Table S3). It should be noted that the maximum efficiency value, $\eta = 53\%$ was measured for the configuration comprising $4 \times 4 \times 3$ unit cells with a wall thickness of 526 μm , while in the other cases, the wall thickness was only 394 μm . This indicates that at smaller length scales (close to the resolution of the 3D printer) process-induced size-dependent mechanical behaviour of the ligaments influences the energy absorption efficiency.

Among the three materials and printing techniques employed, the Gyroid structure consistently exhibits the highest energy absorption efficiency across all relative densities. The Octet truss structure achieves comparable values at higher relative densities when using PlasGray, while the Kelvin lattice made of PA12 shows similar efficiency at a relative density of 0.23. The trend further confirms that structures dominated by stretching, such as SC and Gyroid, perform better in terms of stiffness and strength. The Octet structure shows enhanced energy absorption efficiency at higher densities.

Numerical analyses were conducted on a select set of previously tested lattice structures. Firstly, four different lattice structures with a constant relative density of 0.23 (Table S1 and Table S2 row 1) were analysed using the material properties obtained for bulk PA12 and VeroWhite samples. Secondly, a set of Gyroid lattice structures with varying relative densities (as summarised in Table S2) considering material properties of PlasGray were examined. The numerical results of the PA12 lattice structures with a relative density of 0.23 (Fig. 6e) under compression reveal an excellent agreement with the experimental findings. However, it should be noted that the FE predictions of the Octet lattice structure showed higher strength and stiffness than those obtained from experiments. This discrepancy can be attributed to the

Table 4 – Experimental vs. Numerical: Mechanical performance of lattice structures processed by MJ AM using VeroWhite for $4 \times 4 \times 3$ unit cell configuration and $\bar{\rho} = 0.23$.

VeroWhite	E [MPa]		σ [MPa]		W [MJ/m ³]		η	
	EXP	FEA	EXP	FEA	EXP	FEA	EXP	FEA
Octet	42.8 ± 2.9	88.7	2.1 ± 0.2	4.5	0.98 ± 0.08	2.9	0.47 ± 0.04	0.65
Kelvin	52.2 ± 3.3	91.9	2.6 ± 0.2	4.1	0.69 ± 0.12	2.2	0.27 ± 0.07	0.53
Gyroid	65.7 ± 5.9	88.1	3.2 ± 0.3	4.1	1.67 ± 0.11	2.5	0.53 ± 0.01	0.62
SC	116.6 ± 6.9	193.6	4.2 ± 0.2	7.5	1.77 ± 0.11	4.6	0.42 ± 0.01	0.62

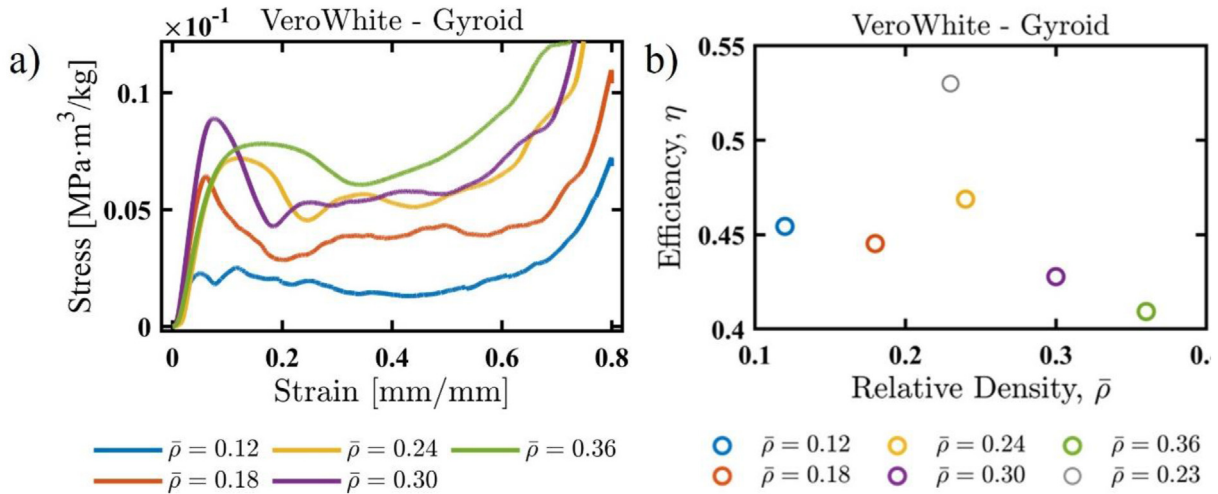


Fig. 9 – Measured performance of Gyroid lattices under quasi-static compression processed by MJ AM using VeroWhite: a) stress-strain response for different relative densities and b) energy absorption efficiency as a function of relative density.

delicate structural members in the outer layers of the lattice, which were only half the size of the inner ones, making them more susceptible to damage and premature failure during experiments. Increasing the number of repeating unit cells could mitigate this issue. For larger strains, the predicted curves remain in good agreement with the experimental data, although the transition from the plateau regime to the densification regime is more abrupt in the numerical analysis. Furthermore, the analysis of energy absorption efficiency confirms the same trend observed from experiments, where

the Gyroid structure outperforms other structures. However, the magnitudes of the energy absorption efficiency values in the experiments are slightly lower (Table 3).

Fig. 10 depicts the von Mises stress distribution under uniaxial compression for both individual unit cells and the lattice structure composed of $4 \times 4 \times 3$ unit cells. The stress distribution provides valuable insights into the mechanical behaviour of the lattice structures. In the Gyroid structure, a uniform stress contribution is observed, indicating the absence of stress concentrations. This aligns with the

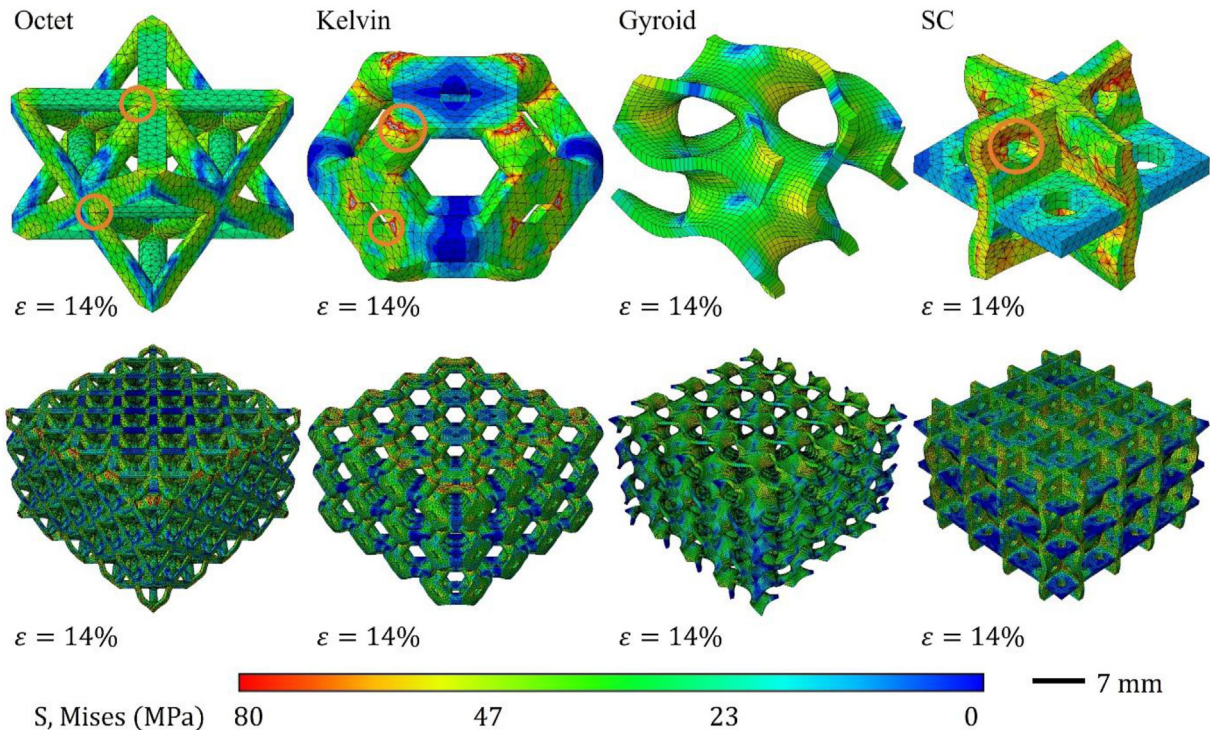


Fig. 10 – Von Mises stress contribution in PA12 lattice structures under quasi-static compression for $\bar{\rho} = 0.23$. Top row shows different unit cells, and the bottom row shows corresponding lattice structure.

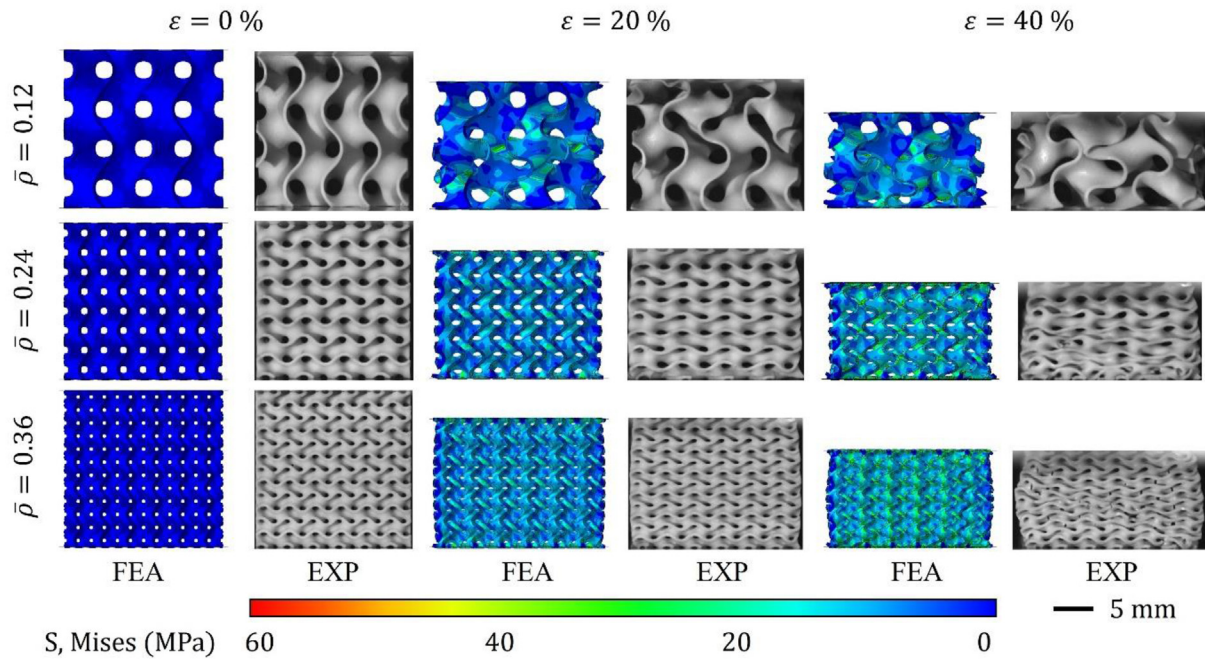


Fig. 11 – Comparison of deformation maps obtained from FEA and experiments for the Gyroid lattice printed using PlasGray under uniaxial compression. The FE maps show the von Mises stress.

previously observed uniform stress-strain response. On the other hand, the Kelvin unit cell exhibits higher stress concentrations in the vertical struts, while the horizontal struts bear a lesser load. Additionally, stress peaks exceeding the yield stress in compression (~ 40 MPa) observed for PA12 are evident at the junctions, as indicated in the figure. This leads to subsequent crack initiation and ductile failure. The Octet unit cell demonstrates a uniform stress distribution with stress peaks concentrated at the joints, as depicted in the plot. In the case of the SC structure, stress is predominantly concentrated in the vertical walls, whereas the horizontal members experience relatively lower stress levels. The vertical walls tend to buckle, resulting in maximum stresses on the stretched side. Furthermore, stress concentrations are observed at the vertical holes, which were introduced to clean the model after printing. However, the magnitude of these peaks is smaller compared to those caused by buckling. Globally, stress concentrations are most prominent in the outer layers of all the structures, reflecting the mechanical behaviour of these regions.

The FE stress-strain results obtained for lattice structures using the VeroWhite material model exhibit a good agreement

with the experimental findings. However, it should be noted that certain mechanical properties, such as Young's modulus and strength, consistently exhibit an overprediction, ranging from 1.2 to 2.2 times the experimental values. Interestingly, only the Gyroid structure exhibits a good agreement between numerical and experimental data. Although the material model showcased accurate predictions when applied to macro-scale samples, it fails to capture the mechanical behaviour of lattice structures composed entirely of micro-scale features. This discrepancy is attributable to the process-induced size-effect anomaly encountered with photosensitive polymers, and such size-dependent variation in curing kinetics affects the mechanical properties. This has been demonstrated by performing tensile and compression tests on bulk macroscale and microscale PlasGray specimens (Please refer to Fig. 3 for the macroscale response and Fig. 4 for the microscale response of PlasGray bulk material under tension and compression). The superior performance of the Gyroid structure can be attributed to its manufacturing conditions, as it consists of one large, continuous surface that eliminates stress concentrations typically found at corners or junctions, as demonstrated in this study. Despite this

Table 5 – Summary of mechanical performance obtained both from FEA and experiments for Gyroid lattice structures fabricated using PlasGray, indicating the % difference between both.

$\bar{\rho}$	E [MPa]			σ [MPa]			W [kJ/m ³]			H		
	FEA	EXP	%	FEA	EXP	%	FEA	EXP	%	FEA	EXP	%
0.12	4.6	4.32	+6%	0.29	0.15	+49%	188	94	+50%	0.64	0.61	+5%
0.18	8.2	8.65	-5%	0.76	0.50	+34%	466	262	+44%	0.56	0.53	+5%
0.24	13.3	13.61	-2%	1.26	0.96	+24%	862	534	+38%	0.54	0.53	+3%
0.3	16.8	16.85	+0%	1.72	1.33	+23%	1067	906	+15%	0.51	0.49	+4%
0.36	25.3	27.18	-7%	2.51	1.93	+23%	1643	1221	+26%	0.51	0.5	+2%

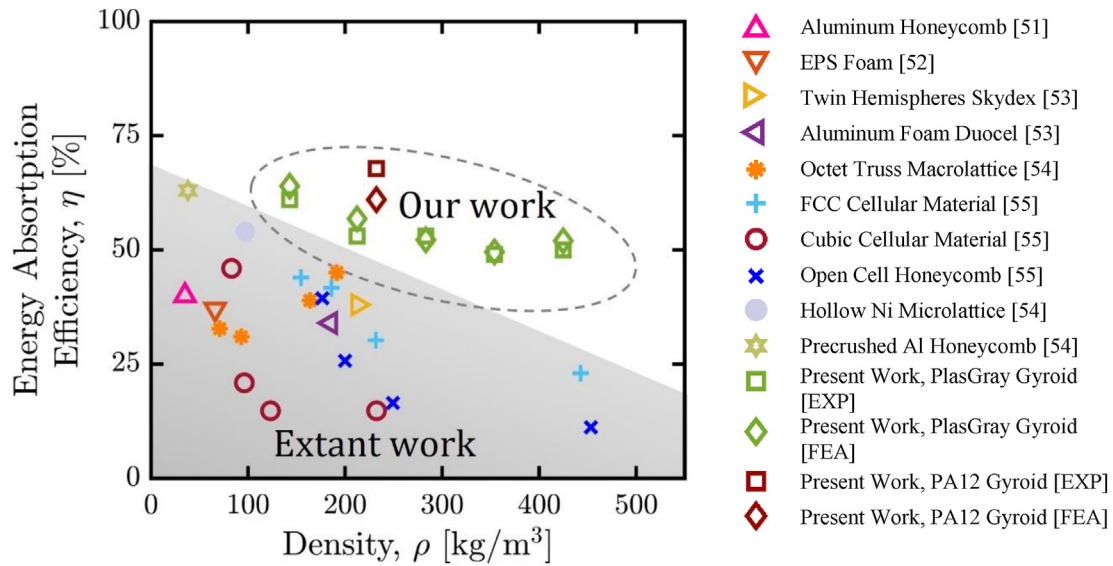


Fig. 12 – Energy absorption efficiency of our AM-enabled micro-architected lattices in comparison with extant works [51–55].

discrepancy, the predicted stress-strain response follows the same trend as the experimental results. Consistently, the PA12 Gyroid lattice structures showed a superior performance in terms of energy absorption efficiency, as revealed in both the simulations and experiments (Tables 3 and 4).

A comprehensive two-step analysis was conducted on microscale Gyroid lattice structures 3D printed using the PlasGray for a range of relative densities, $\bar{\rho} = \{0.12, 0.18, 0.24, 0.3, 0.36\}$. The analysis aimed to examine the buckling behaviour and account for imperfections in the structure's geometry. In the first step, the first three eigenmodes of the structures were determined to analyse their buckling characteristics. The second step involved an explicit analysis that considered the imperfections identified in the previous step. This explicit analysis ensured that the stiffness of the structure was not artificially increased, as premature failure by buckling was taken into account. Fig. 11 presents a comparison of deformation maps obtained from finite element analysis and experiments for the PlasGray Gyroid lattice under uniaxial compression. The maps showcase the distribution of von Mises stress concentrations, highlighting areas of localized stress. Furthermore, the stress-strain response obtained through FEA is compared with the experimental results.

The numerical values for Young's moduli demonstrate excellent agreement with the experimental results, with an average deviation of only 2%. Following the material's yield point, the stress reduction occurs at a slightly slower rate compared to the experimental observations. As a result, higher maximum stresses are reached, leading to increased energy absorption, as indicated in Table 5. Notably, the stress peaks in the simulations occur at similar positions as observed experimentally, and the onset of densification is also observed at strains of approximately 60%. The efficiency of the lattice structures is remarkably well-matched with the experimental data, with an average deviation of only 4%. This trend shows a decrease in efficiency with increasing relative density. For instance, a relative density of 0.12 corresponds to

an efficiency value of 64%, while a relative density of 0.36 corresponds to an efficiency value of 51%.

When testing cellular materials, small samples may have different material properties than large samples [48]. The material properties used to calibrate the FE model were obtained from microscale tensile tests, with a gauge length of ~ 1 mm and a cross section of 0.09 mm^2 . This approach demonstrated a significantly improved predictive capability compared to a previously calibrated material model based on macroscale structures. Curing kinetics at smaller length scales differ from those at larger length scales, suggesting the need for additional post-curing to remove process-induced size-effect anomaly [49,50]. However, a thorough investigation of this aspect is left to subsequent study. Buckling behaviour was found to have a negligible influence on relative densities above 0.18 (Fig. S2) with a slight reduction in initial stiffness and strength by up to 10% and a delayed densification onset observed at lower densities. Irrespective of the dimensional influences, the difference between simulation and experiment for the efficiency is within $\sim 4\%$, in fact, it shows the same trend of higher energy absorption efficiency at low relative densities. Notably, the lattices demonstrated herein surpass the energy absorption attributes of energy absorbing lightweight lattice structures reported in recent studies across a wide range of relative densities (Fig. 12).

4. Conclusion

In this study, the deformation mechanisms and mechanical performance of truss-, shell-, and plate-lattice structures processed by three different 3D printing techniques were analysed both via experiments and finite element modelling. Octet and Kelvin truss-lattices, Gyroid shell-lattice, and SC, BCC, and FCC plate-lattices were investigated. Three different materials, namely PlasGray printed using digital light processing, PA12 printed using selective laser sintering, and

VeroWhite printed using material jetting were utilised in the study. Various sets of lattice structures with both constant and varying relative densities ranging from 0.06 to 0.4 were printed. Quasi-static compression tests were conducted to evaluate the stiffness, strength, energy absorption capacity, and energy absorption efficiency of each lattice structure.

In terms of stiffness and strength under axial loading conditions, the SC structure exhibited superior performance compared to other structures with the same relative density for all materials and printing techniques employed. For PlasGray with a relative density of 0.3, the SC structure displayed Young's modulus values 2.1–14.5 times higher than any other structure in the study. Similarly, for strength and energy absorption, the SC structure outperformed other structures with factors ranging from 1.8 to 15.9 and 1.5–19.6 respectively. Similar trends were observed for PA12 and VeroWhite materials. Following the SC structure, the Kelvin and Gyroid structures showed comparable performance in terms of stiffness and strength for PA12. However, for VeroWhite, the Gyroid structure exhibited significantly better performance than the Kelvin structure, likely due to the brittle nature of VeroWhite material. On the other hand, the Octet structure was most susceptible to fracture after yielding, resulting in a significant drop in the stress for relative densities below 0.3 due to buckling. The BCC and FCC structures showed poor performance, primarily due to their thin feature sizes of 213 μm and 170 μm respectively (using PlasGray). These feature sizes were inadequate for the selected printing processes and machines. Overall, it was observed that stretch-dominated structures generally exhibited superior stiffness and strength compared to bending-dominated structures. The Gyroid lattices exhibit superior energy absorption efficiency compared to other structures. For PlasGray, for the relative density range of $\bar{\rho} = 0.36$ to 0.12, the measured efficiency ranged from $\eta = 49$ to 61%. This means that as the relative density of Gyroid structures decreases their energy absorption capability increases. In the case of PA12, an efficiency of up to $\eta = 68\%$ was achieved at a relative density of $\bar{\rho} = 0.23$.

Using three different calibrated constitutive models-elastic-plastic, Drucker-Prager, and concrete damage plasticity - finite element analyses were conducted on a selected set of lattice structures. Examination of the stress distribution in different unit cells demonstrates that the Gyroid structure exhibits a uniform stress distribution without any localized stress peaks, thanks to its continuous shape. The FE results for microscale lattice structures indicate a size-effect anomaly caused by the manufacturing process in photo-resin-based methods. This anomaly results in discrepancies between experimental and FE results, as observed in the case of VeroWhite. Since the material model for VeroWhite was calibrated using macro-scale test data, the FEA of microscale lattices doesn't yield a predictive capability. We addressed this issue in the context of the DLP technique by identifying constitute parameters through microscale experiments. By doing so, we significantly reduced discrepancies stemming from the size-effect anomaly. Such an approach leads to excellent agreement between experimental and FE results. However, this aspect requires a thorough study and is left to future study. Despite the challenges in direct parameter comparison in some cases, the deformation maps and trends obtained from

experiments remain consistent with FE results. Notably, the FE results confirm the superior energy absorption efficiency of the Gyroid structure, aligning with the experimental findings.

Declaration of competing interest

The authors declare that they have no known competing financial interests or personal relationships that could have appeared to influence the work reported in this paper.

Acknowledgements

This work was supported in part by the EPSRC Centre, funded by the UK Engineering and Physical Sciences Research Council (grant EP/R513222/1) and the University of Glasgow.

Appendix A. Supplementary data

Supplementary data to this article can be found online at <https://doi.org/10.1016/j.jmrt.2023.09.061>.

Supplementary video related to this article can be found at <https://doi.org/10.1016/j.jmrt.2023.09.061>

REFERENCES

- [1] Zheng X, Lee H, Weisgraber T, Shusteff M, DeOtte J, Duoss E, et al. Ultralight, ultrastiff mechanical metamaterials. *Science* 2014;344:1373–7. <https://doi.org/10.1126/science.1252291>. 80.
- [2] Snelling D, Li Q, Meisel N, Williams C, Druschitz A. Lightweight metal cellular structures fabricated via 3D printing of sand cast molds. *Adv Eng Mater* 2015;17. <https://doi.org/10.1002/adem.201400524>.
- [3] Malek S, Raney J, Lewis J, Gibson L. Lightweight 3D cellular composites inspired by balsa. *Bioinspiration Biomimetics* 2017;12. <https://doi.org/10.1088/1748-3190/aa6028>.
- [4] Andrew JJ, Schneider J, Ubaid J, Velmurugan R, Gupta NK, Kumar S. Energy absorption characteristics of additively manufactured plate-lattices under low-velocity impact loading. *Int J Impact Eng* 2021;149:103768. <https://doi.org/10.1016/j.ijimpeng.2020.103768>.
- [5] Ubaid J, Schneider J, Deshpande VS, Wardle BL, Kumar S. Multifunctionality of nanoengineered self-sensing lattices enabled by additive manufacturing. *Adv Eng Mater* 2022;2200194. n/a. <https://doi.org/10.1002/adem.202200194>.
- [6] Lee J-H, Singer J, Thomas E. Micro-/Nanostructured mechanical metamaterials. *Adv Mater* 2012;24:4782–810. <https://doi.org/10.1002/adma.201201644>.
- [7] Jang D, Meza L, Greer F, Greer J. Fabrication and deformation of three-dimensional hollow ceramic nanostructures. *Nat Mater* 2013;12. <https://doi.org/10.1038/nmat3738>.
- [8] Meza L, Das S, Greer J. Strong, lightweight, and recoverable three-dimensional ceramic nanolattices. *Science* 2014;345:1322–6. <https://doi.org/10.1126/science.1255908>.
- [9] Habib FNN, Iovenitti P, Masood SHH, Nikzad M. Fabrication of polymeric lattice structures for optimum energy absorption using Multi Jet Fusion technology. *Mater Des* 2018;155:86–98. <https://doi.org/10.1016/j.matdes.2018.05.059>.
- [10] Andrew JJ, Verma P, Kumar S. Impact behavior of nanoengineered, 3D printed plate-lattices. *Mater Des* 2021;202:109516. <https://doi.org/10.1016/j.matdes.2021.109516>.

- [11] Gibson LJ, Ashby MF. Cellular solids: structure and properties. second ed. Cambridge: Cambridge University Press; 1999. <https://doi.org/10.1017/CBO9781139878326>.
- [12] Lei Y, Mertens R, Ferrucci M, Yan C, Shi Y, Yang S. Continuous graded Gyroid cellular structures fabricated by selective laser melting: design, manufacturing and mechanical properties. *Mater Des* 2018;162. <https://doi.org/10.1016/j.matdes.2018.12.007>.
- [13] Maskery I, Hussey A, Panesar A, Aremu A, Tuck C, Ashcroft I, et al. An investigation into reinforced and functionally graded lattice structures. *J Cell Plast* 2016;53. <https://doi.org/10.1177/0021955X16639035>.
- [14] Wang K, Chang Y-H, Chen Y, Zhang C, Wang B. Designable dual-material auxetic metamaterials using three-dimensional printing. *Mater Des* 2015;67. <https://doi.org/10.1016/j.matdes.2014.11.033>.
- [15] Song J, Zhou W, Wang Y, Fan R, Wang Y, Chen J, et al. Octet-truss cellular materials for improved mechanical properties and specific energy absorption. *Mater Des* 2019;173:107773. <https://doi.org/10.1016/j.matdes.2019.107773>.
- [16] Saha SK, Wang D, Nguyen VH, Chang Y, Oakdale JS, Chen S-C. Scalable submicrometer additive manufacturing. *Science* 2019;366:105–9. 80. <https://doi.org/10.1126/science.aax8760>.
- [17] Schaedler T, Jacobsen A, Torrents A, Sorensen A, Lian J, Greer J, et al. Ultralight metallic microlattices. *Science* 2011;334:962–5. <https://doi.org/10.1126/science.1211649>.
- [18] Köhnen P, Haase C, Bültmann J, Ziegler S, Schleifenbaum JH, Bleck W. Mechanical properties and deformation behavior of additively manufactured lattice structures of stainless steel. *Mater Des* 2018;145:205–17. <https://doi.org/10.1016/J.MATDES.2018.02.062>.
- [19] Kumar S, Parakkal J, Rajkumar A, Schiffer A, Deshpande V. Tunable energy absorption characteristics of architected honeycombs enabled via additive manufacturing. *ACS Appl Mater Interfaces* 2019. <https://doi.org/10.1021/acsami.9b12880>.
- [20] Andrew JJ, Ubaid J, Hafeez F, Schiffer A, Kumar S. Impact performance enhancement of honeycombs through additive manufacturing-enabled geometrical tailoring. *Int J Impact Eng* 2019;134:103360. <https://doi.org/10.1016/j.ijimpeng.2019.103360>.
- [21] Gibson I, Rosen D, Stucker B, et al Rosen D, Stucker B, Khorasani M. Additive manufacturing technologies. Springer; 2021.
- [22] Saptarshi SM, Zhou DC. Chapter 2 - basics of 3D printing: engineering aspects. In: Dipaola M, Wodajo FM, editors. 3D print. Orthop. Surg. Elsevier; 2019. p. 17–30. <https://doi.org/10.1016/B978-0-323-58118-9.00002-6>.
- [23] Azam MU, Schiffer A, Kumar S. Mechanical and piezoresistive behavior of selectively laser sintered MWCNT/UHMWPE nanocomposites. *Compos Part A Appl Sci Manuf* 2023;173:107701. <https://doi.org/10.1016/j.compositesa.2023.107701>.
- [24] Saadi OW, Uddin MA, Schiffer A, Kumar S. Digital light processing of 2D lattice composites for tunable self-sensing and mechanical performance. *Adv Eng Mater* 2023. n/a. <https://doi.org/10.1002/adem.202300473>.
- [25] Ngo TD, Kashani A, Imbalzano G, Nguyen KTQ, Hui D. Additive manufacturing (3D printing): a review of materials, methods, applications and challenges. *Composites Part B* 2018;143:172–96. <https://doi.org/10.1016/j.compositesb.2018.02.012>.
- [26] Verma P, Ubaid J, Varadarajan KM, Wardle BL, Kumar S. Synthesis and characterization of carbon nanotube-doped thermoplastic nanocomposites for the additive manufacturing of self-sensing piezoresistive materials. *ACS Appl Mater Interfaces* 2022;14:8361–72. <https://doi.org/10.1021/acsami.1c20491>.
- [27] Tancogne-Dejean T, Spierings A, Mohr D. Additively-manufactured metallic micro-lattice materials for high specific energy absorption under static and dynamic loading. *Acta Mater* 2016;116:14–28. <https://doi.org/10.1016/j.actamat.2016.05.054>.
- [28] Tancogne-Dejean T, Diamantopoulou M, Gorji M, Bonatti C, Mohr D. 3D plate-lattices: an emerging class of low-density metamaterial exhibiting optimal isotropic stiffness. *Adv Mater* 2018;30:1803334. <https://doi.org/10.1002/adma.201803334>.
- [29] Ye J, Liu L, Oakdale J, Lefebvre J, Bhowmick S, Voisin T, et al. Ultra-low-density digitally architected carbon with a strutted tube-in-tube structure. *Nat Mater* 2021;20:1498–505. <https://doi.org/10.1038/s41563-021-01125-w>.
- [30] Bauer J, Hengsbach S, Tesari I, Schwaiger R, Kraft O. High-strength cellular ceramic composites with 3D microarchitecture. *Proc Natl Acad Sci USA* 2014;111:2453–8. <https://doi.org/10.1073/pnas.1315147111>.
- [31] Wendy Gu X, Greer JR. Ultra-strong architected Cu meso-lattices. *Extrem. Mech. Lett.* 2015;2:7–14. <https://doi.org/10.1016/J.EML.2015.01.006>.
- [32] Maskery I, Aboulkhair NT, Aremu AO, Tuck CJ, Ashcroft IA. Compressive failure modes and energy absorption in additively manufactured double gyroid lattices. *Addit Manuf* 2017;16:24–9. <https://doi.org/10.1016/J.ADDMA.2017.04.003>.
- [33] Andrew J, Schneider J, Schiffer A, Hafeez F, Kumar S. Dynamic crushing of tailored honeycombs realized via additive manufacturing. *Int J Mech Sci* 2022;219:107126. <https://doi.org/10.1016/j.ijmecsci.2022.107126>.
- [34] Uribe-Lam E, Treviño-Quintanilla CD, Cuan-Urquizo E, Olvera-Silva O. Use of additive manufacturing for the fabrication of cellular and lattice materials: a review. *Mater Manuf Process* 2021;36:257–80. <https://doi.org/10.1080/10426914.2020.1819544>.
- [35] Sculpteo, 3D printing material: VeroWhite resin. 2019. <https://www.sculpteo.com/en/materials/polyjet-resin-material/verowhite-polyjet-resin-material/>. [Accessed 15 June 2019].
- [36] Schneider J, Kumar S. Multiscale characterization and constitutive parameters identification of polyamide (PA12) processed via selective laser sintering. *Polym Test* 2020;106357. <https://doi.org/10.1016/J.POLYMERTESTING.2020.106357>.
- [37] 3DSYSTEMS. DuraForm PA plastic. 2019. https://www.3dsystems.com/sites/default/files/2017-01/DS_DuraForm_PA_US_0.pdf. [Accessed 13 October 2019].
- [38] Dadbakhsh S, Verbelen L, Verkinderen O, Strobbe D, Van Puyvelde P, Kruth J-P. Effect of PA12 powder reuse on coalescence behaviour and microstructure of SLS parts. *Eur Polym J* 2017;92. <https://doi.org/10.1016/j.eurpolymj.2017.05.014>.
- [39] Deshpande VS, Fleck N, Ashby M. Effective properties of the octet-truss lattice material. *J Mech Phys Solid* 2001;49:1747–69. [https://doi.org/10.1016/S0022-5096\(01\)00010-2](https://doi.org/10.1016/S0022-5096(01)00010-2).
- [40] Dixit T, Al-Hajri E, Paul MC, Nithiarasu P, Kumar S. High performance, microarchitected, compact heat exchanger enabled by 3D printing. *Appl Therm Eng* 2022;210:118339. <https://doi.org/10.1016/j.applthermaleng.2022.118339>.
- [41] Schoen AH. Infinite periodic minimal surfaces without self-intersections. 1970.
- [42] Standard test method for compressive properties of rigid cellular plastics. 2023. <https://www.astm.org/d1621-16.html>.
- [43] Li QM, Magkiriadis I, Harrigan JJ. Compressive strain at the onset of densification of cellular solids. *J Cell Plast* 2006;42:371–92. <https://doi.org/10.1177/0021955X06063519>.

- [44] Extended drucker-prager models - SIMULIA user assistance 2023. 2023. https://help.3ds.com/2023/english/dssimulia_established/SIMACAEMATRefMap/simamat-c-druckerprager.htm?contextscope=all.
- [45] Logakannan KP, Ruan D, Rengaswamy J, Kumar S, Ramachandran V. Fracture locus of additively manufactured AlSi10Mg alloy. *Thin-Walled Struct* 2023;184:110460. <https://doi.org/10.1016/j.tws.2022.110460>.
- [46] Lubliner J, Oliver J, Oller S, Onate E. A plastic-damage model for concrete. *Int J Solid Struct* 1989;25:299–326. [https://doi.org/10.1016/0020-7683\(89\)90050-4](https://doi.org/10.1016/0020-7683(89)90050-4).
- [47] Abaqus, defining concrete damaged plasticity - SIMULIA user assistance 2023. 2023. https://help.3ds.com/2023/english/dssimulia_established/SIMACAECAERefMap/simacae-m-PrpMechanicalPlasticConcretedamaged-sb.htm?contextscope=all.
- [48] Yoder M, Thompson L, Summers J. Size effects in lattice structures and a comparison to micropolar elasticity. *Int J Solid Struct* 2018;143. <https://doi.org/10.1016/j.ijsolstr.2018.03.013>.
- [49] Riccio C, Civera M, Grimaldo Ruiz O, Pedullà P, Rodriguez Reinoso M, Tommasi G, et al. Effects of curing on photosensitive resins in SLA additive manufacturing. *Appl. Mech.* 2021;2:942–55. <https://doi.org/10.3390/applmech2040055>.
- [50] Zhao J, Yang Y, Li L. A comprehensive evaluation for different post-curing methods used in stereolithography additive manufacturing. *J Manuf Process* 2020;56:867–77. <https://doi.org/10.1016/J.JMAPRO.2020.04.077>.
- [51] Liu Y, Schaedler T, Chen X. Dynamic energy absorption characteristics of hollow Microlattice structures. *Mech Mater* 2014;77. <https://doi.org/10.1016/j.mechmat.2014.06.008>.
- [52] Caserta GD, Iannucci L, Galvanetto U. Shock absorption performance of a motorbike helmet with honeycomb reinforced liner. *Compos Struct* 2011;93:2748–59. <https://doi.org/10.1016/j.compstruct.2011.05.029>.
- [53] De Sousa RA, Goncalves D, Coelho R, Teixeira-Dias F. Assessing the effectiveness of a natural cellular material used as safety padding material in motorcycle helmets. *Simulation-Transactions Soc. Model. Simul. Int.* 2012;88:580–91. <https://doi.org/10.1177/0037549711414735>.
- [54] Schaedler TA, Ro CJ, Sorensen AE, Eckel Z, Yang SS, Carter WB, et al. Designing metallic microlattices for energy absorber applications. *Adv Eng Mater* 2014;16:276–83. <https://doi.org/10.1002/adem.201300206>.
- [55] Mieszala M, Hasegawa M, Guillonneau G, Bauer J, Raghavan R, Frantz C, et al. Micromechanics of amorphous metal/polymer hybrid structures with 3D cellular architectures: size effects, buckling behavior, and energy absorption capability. *Small* 2016;13. <https://doi.org/10.1002/smll.201602514>.